



A high-performance and durable direct NH₃ tubular protonic ceramic fuel cell integrated with an internal catalyst layer

Yuxin Pan^a, Hua Zhang^a, Kang Xu^a, Yucun Zhou^b, Bote Zhao^{a,b}, Wei Yuan^c, Kotaro Sasaki^d, YongMan Choi^{e,*}, Yu Chen^{a,f,**}, Meilin Liu^{b,*}

^a School of Environment and Energy, South China University of Technology, Guangzhou 510006, China

^b School of Materials Science and Engineering, Georgia Institute of Technology, 771 Ferst Dr NW, Atlanta, GA 30332-0245, USA

^c School of Mechanical and Automotive Engineering, South China University of Technology, Guangzhou 510640, China

^d Chemistry Department, Brookhaven National Laboratory, Upton, NY 11973, USA

^e College of Photonics, National Yang Ming Chiao Tung University, Tainan 71150, Taiwan

^f Guangdong Provincial Key Laboratory of Atmospheric Environment and Pollution Control, South China University of Technology, Guangzhou Higher Education Mega Centre, Guangzhou 510006, PR China

ARTICLE INFO

Keywords:

Protonic ceramic fuel cells
Tubular cells
Ammonia fuel
Catalytic layer

ABSTRACT

Nickel-based cermet anode-supported protonic ceramic fuel cells (PCFCs) show great potential for direct utilization of ammonia. However, the insufficient activity of anode and the deterioration of anode activity/durability caused by the undesired interaction between nickel and ammonia greatly limit the application. Here, we report tubular PCFCs embedded with a catalytic iron layer. Such cells show peak power densities of 1.507 W cm⁻² and 1.078 W cm⁻² at 700 °C when using H₂ and NH₃ as fuel, respectively, which are the highest tubular PCFC performance so far ever reported. In addition, the stability of cells with the catalyst layer has been dramatically enhanced when compared with that of cells without the catalyst layer. The enhancement of activity and durability is attributed to the catalytic activity of iron for ammonia decomposition, through which the direct contact between nickel and ammonia has been minimized and the anode structure has therefore been protected.

1. Introduction

Solid oxide fuel cells (SOFCs) can directly convert the chemical energy of fuels to electricity [1–4] and have been considered as one of the most promising energy devices in the future because of the relatively high energy conversion efficiency, low emissions, and huge fuel flexibility [5–8]. Among them, protonic ceramic fuel cells (PCFCs) are currently more attractive than oxygen ions-based SOFC due to the high conductivity of protons, enabling operations at intermediate temperatures. Although hydrogen is frequently used as fuel for PCFCs, the wide deployment of hydrogen energy is hindered by the large financial investment and safety risk in storage and transportation [9] due to the technological difficulties in liquefaction or compression of hydrogen [10]. Therefore, alternative fuels such as hydrocarbons or ammonia have been proposed for PCFCs.

Since the very first successful report of utilizing ammonia as fuel in a ceramic fuel cell system [11], the potential of ammonia has been

gradually recognized by the SOFC community. As a carbon-free hydrogen carrier, ammonia has a high content of hydrogen and can be readily decomposed to H₂ and N₂ over traditional nickel-based cermet anodes at operating temperatures (500–800 °C) [12]. In addition, ammonia can not only be liquefied in mild conditions [13] but also be widely used as a commercial chemical in the industry [14], making it a possible candidate as an alternative fuel for PCFCs. Numerous efforts have been devoted to the studies of ammonia-fueled PCFCs. For example, an early attempt by Xie et al. [15] demonstrated the feasibility of ammonia-fueled PCFCs, resulting in a peak power density of 315 mW cm⁻² at 700 °C. Aoki et al. [16] developed an ammonia-fueled PCFC based on the BaZr_{0.1}Ce_{0.7}Y_{0.2}O_{3-δ} electrolyte and Pd solid anode, which delivered a high output of 580 mW cm⁻² at 600 °C. Yang et al. [17] investigated the electrochemical and catalytic properties of a Ni-BaCe_{0.75}Y_{0.25}O_{3-δ} anode, exhibiting a higher ammonia decomposition catalytic activity over the Ni-YSZ (8 mol% Y₂O₃ stabilized ZrO₂) or Ni-Ce_{0.9}Gd_{0.1}O_{1.95} anodes. Still, the efforts on developing ammonia

* Corresponding authors.

** Corresponding author at: School of Environment and Energy, South China University of Technology, Guangzhou 510006, China.

E-mail addresses: ymchoi@nctu.edu.tw (Y. Choi), eschenyu@scut.edu.cn (Y. Chen), meilin.liu@mse.gatech.edu (M. Liu).

<https://doi.org/10.1016/j.apcatb.2022.121071>

Received 15 September 2021; Received in revised form 30 December 2021; Accepted 4 January 2022

Available online 7 January 2022

0926-3373/© 2022 Elsevier B.V. All rights reserved.

PCFCs are very limited and the present achievements are yet to be satisfying. In particular, studies on the durability of ammonia PCFCs are insufficient. Therefore, more efforts are greatly necessary to develop high-performance and durable ammonia PCFCs.

Power generation using NH_3 -fueled PCFC systems mainly consists of four steps: (i) adsorption of NH_3 on the anode surface; (ii) catalytic decomposition of NH_3 into H_2 and N_2 ; (iii) production of protons and electrons from the electrochemical reaction of H_2 ; (iv) protons transport through the dense electrolyte and electrons transport through an external circuit to the cathode [18]. As a key component for the anode, nickel shows a high electrical conductivity and an excellent catalytic activity towards the electrochemical reaction of H_2 . Furthermore, nickel exhibits an efficient catalytic activity for ammonia decomposition, indicating that nickel-based anodes have great potential for ammonia-fueled ceramic fuel cells. However, cell durability in ammonia is a big concern [19], particularly due to the nitridation of nickel grains. Nitridation is dependent on experimental conditions (i.e., pressure and temperature), but it causes detrimental changes to the anode microstructure and consequently the degradation of cell performance [20]. A highly effective strategy to mitigate the crucial issue and maintain a stable operation of fuel cells is to decompose NH_3 into H_2 before interacting with nickel anodes, minimizing the direct exposure of nickel to pure ammonia. The addition of another catalytic layer can facilitate the decomposition reaction of ammonia, a similarly practical approach for the development of direct hydrocarbons fueled SOFCs, where an internal catalyst layer is used to decompose hydrocarbons to H_2 [21]. For practical preparation of the additional catalyst layer for efficient NH_3 decomposition, a tubular configuration has been proposed owing to its effective integration of additional catalysts with nickel-based cermet backbone, suggesting that tubular cells may have inherent advantages to utilize ammonia fuel [22]. Besides, tubular cells also provide high mechanical strength, outstanding thermal-cycle stability, and easy assembling into stacks [23,24], which make tubular cells promising for practical scaling up and commercialization. In particular, most of the reported NH_3 -fueled tubular fuel cells are based on conventional oxygen-ion conducting SOFCs. On the contrary, tubular PCFCs operating in ammonia fuel are still undeveloped, and very few reports are available in the literature.

Herein, in the present study, tubular PCFCs based on a $\text{Ni-BaZr}_{0.1}\text{Ce}_{0.7}\text{Y}_{0.1}\text{Yb}_{0.1}$ (BZCYYb) anode support and a BZCYYb electrolyte have been successfully fabricated via cost-effective methods of phase inversion and dip-coating. In particular, outstanding cell performances have been achieved in both hydrogen and ammonia, showing peak power densities of 1.507 W cm^{-2} and 1.078 W cm^{-2} at 700°C , respectively. Furthermore, the durability of cells in ammonia has been significantly improved by the simple addition of an internal catalytic iron layer. To complement the experimental findings, density functional theory (DFT) based simulations were carried out along with thermodynamic characteristics by calculating Gibbs free energies under experimental conditions. The theoretical analyses verify that the extraordinary stability by adding the catalytic iron layer may result from minimizing the direct interaction of nickel and ammonia, avoiding its nitride formation. This systematic rational elucidation of the novel direct NH_3 tubular PCFC's superior performance with excellent stability over the conventional Ni-based configuration can be applied to other carbon-free fuels like hydrazine, widely extending PCFCs applications.

2. Experimental section

2.1. Synthesis of materials

BZCYYb powders were synthesized through a solid-state reaction method [25]. The stoichiometric ratio of BaCO_3 , ZrO_2 , CeO_2 , Y_2O_3 , Yb_2O_3 (all purchased from Shanghai Macklin Biochemical Co. Ltd.) were mixed and ball-milled in ethanol for 24 h. After drying, the mixed powders were pressed into a pellet under 10 MPa and calcined at 1100°C

for 12 h. The above steps of ball-milling, pressing and calcination were repeated two times to obtain the final BZCYYb powders with pure phase. $\text{PrBa}_{0.5}\text{Sr}_{0.5}\text{Co}_{1.5}\text{Fe}_{0.5}\text{O}_{5+\delta}$ (PBSCF) cathode was synthesized by a solution combustion method. The stoichiometric ratio of $\text{Pr}(\text{NO}_3)_3 \cdot 6\text{H}_2\text{O}$, $\text{Ba}(\text{NO}_3)_2$, $\text{Sr}(\text{NO}_3)_2$, $\text{Co}(\text{NO}_3)_2 \cdot 6\text{H}_2\text{O}$, and $\text{Fe}(\text{NO}_3)_3 \cdot 6\text{H}_2\text{O}$ were selected as raw materials and dissolved in deionized water, along with the proper amount of glycine and citric acid (CA) as complexing agent. The molar ratio of glycine: CA: total metal ions was 0.75: 0.75: 1. Water in the solution was evaporated under constant stirring and heating at 80°C , by which a transparent gel was obtained. The gel was then heated to 300°C in an oven for complete combustion. The remaining ashes were further heated to 900°C for 2 h.

2.2. Fabrication of tubular cells

The preparation procedures of the tubular cell (Ni-BZCYYb / BZCYYb / PBSCF) were schematically shown in Fig. 1a. A phase inversion technique was applied to fabricate the anode substrate. In brief, an anode slurry was obtained by the ball-milling of NiO and BZCYYb powders in an organic solution for 24 h. More specifically, 27 g BZCYYb, 40.5 g NiO, 3 g polyethersulfone (PES), 0.75 g polyvinyl pyrrolidone (PVP), and 18 g N-Methyl pyrrolidone (NMP) were mixed together. The slurry was then dip-coated on a glass rod (with a diameter of 4 mm), followed by the immediate immersion in water for 10 h. Phase inversion took place as mass exchanged between the slurry and water. As a result, the slurry eventually solidified and became a raw tube. After peeling off from the glass rod and drying overnight in ambient air, the raw tube was heated to 1000°C to obtain the anode substrate. An anode functional layer (AFL) and an electrolyte layer were sequentially dip-coated on the anode substrate. Before the fabrication of AFL and electrolyte, wax was applied to seal one end of the tube, preventing the contact between the inner tube and the solution for dip-coating. Wax was then removed by heating in a drying oven at 70°C . The tube with AFL and electrolyte layer was co-sintered at 1450°C for 5 h. A cathode slurry, consisting of 55.6 wt% PBSCF, 42.2 wt% terpineols, and 2.2 wt% ethyl cellulose, was then brush-painted on the surface of the electrolyte. The cell was heated to 950°C for 2 h to achieve a good adhesion between the electrolyte and the cathode. Finally, a catalytic layer was added by painting a slurry of iron trioxide (containing 44.4 wt% Fe_2O_3 , 11.2 wt% graphite, 42.2 wt% terpineols, and 2.2 wt% ethyl cellulose) on the inner wall. The final tubular cell with an iron layer (denoted as Fe-cell) is represented in Fig. 1b, and the inner architecture and cross-sectional scanning electron microscope image of the tube were presented in Fig. 1c. In addition, tubular cells fabricated by the same methods except for the addition of a catalytic layer were also produced for comparison and denoted as bare cell.

2.3. Characterization methods

Single-cell tests were carried out in a homemade testing setup. To collect the current, silver wires were attached to the inner wall of the tube and the surface of the cathode, respectively, using a silver paste (DAD-87). The silver wire was made into a coil shape, which can precisely fit into the inside of the tube. The catalyst slurry was then painted inside the tube after adding the silver wire. Electrochemical performances were conducted by using an electrochemical work station (Princeton PARSTAT MC 200) after a reduction in hydrogen for 1 h at the anode side, using pure hydrogen or pure ammonia as fuels and ambient air as oxidant. Product gases were analyzed during cell testing, while the decomposition rate of ammonia was determined by the content of nitrogen using gas chromatography (Huifen GC-7820) and a gas flow meter. In the conversion rate testing, the flow rate of ammonia to the cells was controlled at 20 sccm, using a gas flowmeter. The length of the tubes was retained at 3.5 cm. The inner diameter was 3 mm. The thickness of the catalyst layer was around $25 \mu\text{m}$. The surface area of the iron powder after electrochemical testing was determined as $1.58 \text{ m}^2/\text{g}$,

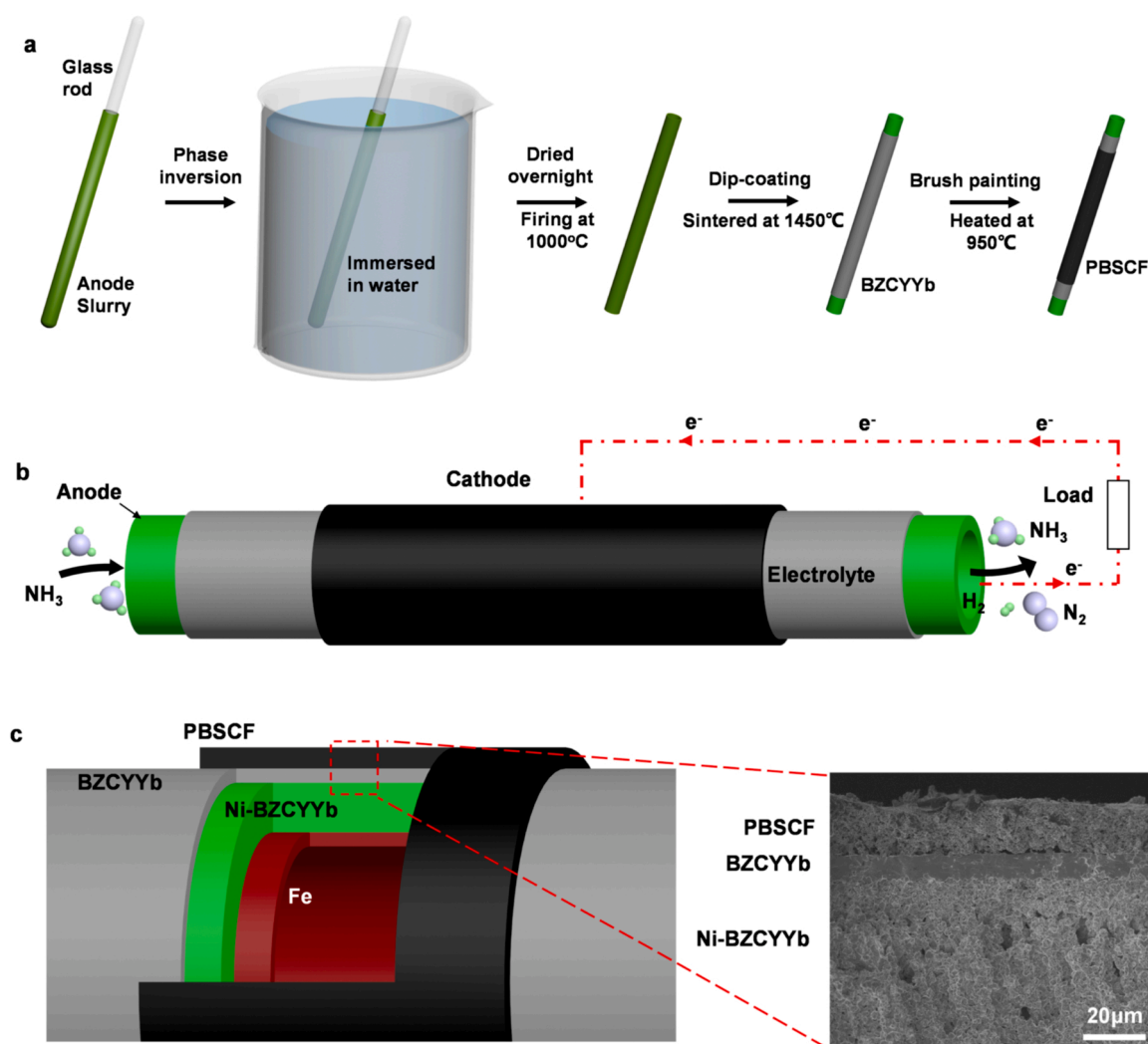


Fig. 1. (a) Schematics of the fabrication process of a tubular cell; (b) schematics of a tubular cell using direct ammonia as the fuel; (c) schematics of the inner architecture of the tube and a scanning electron micrograph of the actual cell consisting of a Ni-BZCYYb anode, a BZCYYb electrolyte, and a PBSCF cathode.

from a Brunauer-Emmett-Teller (BET) measurement. Microstructures and morphologies of the tested cells were observed by a scanning electron microscope (SEM, Hitachi SU8010). Parts of the anodes from the cells after electrochemical testing were ground into powders and the phase structure of the samples was characterized by X-ray diffraction (XRD, Tongda TD-3500) using Cu-K α as a radiation source.

2.4. Computational details

Spin-polarized density functional theory (DFT) calculations were carried out using the Vienna Ab initio Simulation Package (VASP) [26, 27] to examine the outstanding performance and stability of the direct NH₃-fueled protonic ceramic fuel cell using iron layer-added Ni/BZCYYb. We used Perdew-Burke-Ernzerh (PBE) functional [28] and the projector augmented plane wave (PAW) method [29]. The Monkhorst-Pack grid [30] with (3 × 3 × 3) and (3 × 3 × 1) was used for bulk and slab calculations, respectively, while a kinetic energy cutoff for 415 eV was applied. For the NH₃ decomposition processes, (2 × 2) four-layered surfaces of Ni (111) (16 Ni atoms), FeNi (111) (8 Fe and 8 Ni atoms), and Fe(110) (16 Fe atoms) with a vacuum space of 15 Å were applied (*i.e.*, coverage of 1/4). The two bottom layers were fixed to the bulk parameters. The adsorption energy of atomic nitrogen on a surface was calculated by $E_{\text{ads,N}} = E(\text{N-surface}) - E(\text{surface}) - E(\text{N}_2)/2$. While $E(\text{N-surface})$ and $E(\text{surface})$ are calculated electronic energies for

adsorbed N on a surface and its blank surface, respectively, $E(\text{N}_2)$ is that for gas-phase nitrogen. The d-band centers of surfaces were calculated using the average energy of projected density of states (PDOSs) of the d-orbitals of bare metal surfaces [31]. The DMol³ module [32] implemented in the Materials Studio package was used to calculate Gibbs's free energies using the optimized geometries from VASP. The double numerical polarization (DNP) 3.5 basis, the effective core potentials (ECP), and the PBE exchange-correlation functional were applied.

3. Result and discussion

3.1. Microstructure of the tubular cells

Shown in Fig. 2 are SEM images of different parts of the tubular cell after electrochemical testing. As indicated by the overall cross-section of the cell in Fig. 2a, the thickness of the tube wall was around 500 μm. The thickness of the tube wall plays a pivotal role in the mechanical strength of the tube, which was greatly influenced by the viscosity of the original anode slurry in the phase inversion process. By adjusting the mass loading of ceramic powders (NiO-BZCYYb) in the slurry, a robust tube was obtained.

Straight finger-like pores with a few dozen micrometers in length can be found between the anode supporting layer and electrolyte, as shown in Fig. 2a and b. It is a typical structure resulting from the phase

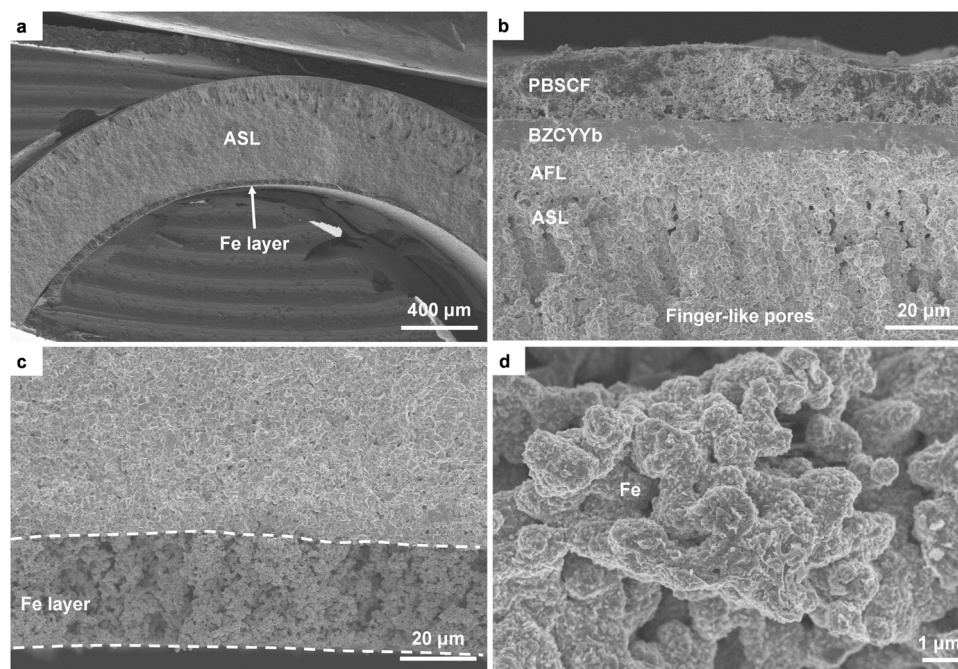


Fig. 2. Typical SEM images of the tubular cell: (a) an overall cross-section of the tube; (b) an enlarged view of the cell with ASL, AFL, BZCYYb, and PBSCF layer; (c) a detailed SEM image of the catalytic iron layer; (d) a close view of the iron surface after testing in ammonia.

inversion process [33], through which an asymmetric membrane containing a skin layer, a finger-like pores layer, and a porous sponge layer can be obtained. BZCYYb electrolyte and PBSCF cathode with a thickness of 8 μm and 20 μm can be observed respectively in the enlarged view near the electrolyte.

A catalytic iron layer with a few dozen of micrometers in thick was marked by the dotted lines in Fig. 2c, indicating that the internal

catalytic layer was successfully added and well attached to the inner wall of the tube after electrochemical testing. Besides, macro voids were found within the iron layer, which was induced by the removal of graphite and organic components in the original iron trioxide slurry. Such macro voids mitigated the negative effect of the additional layer and allowed the smooth diffusion of fuel gases to the anode bulk. The morphology of iron surfaces after testing in ammonia was presented in

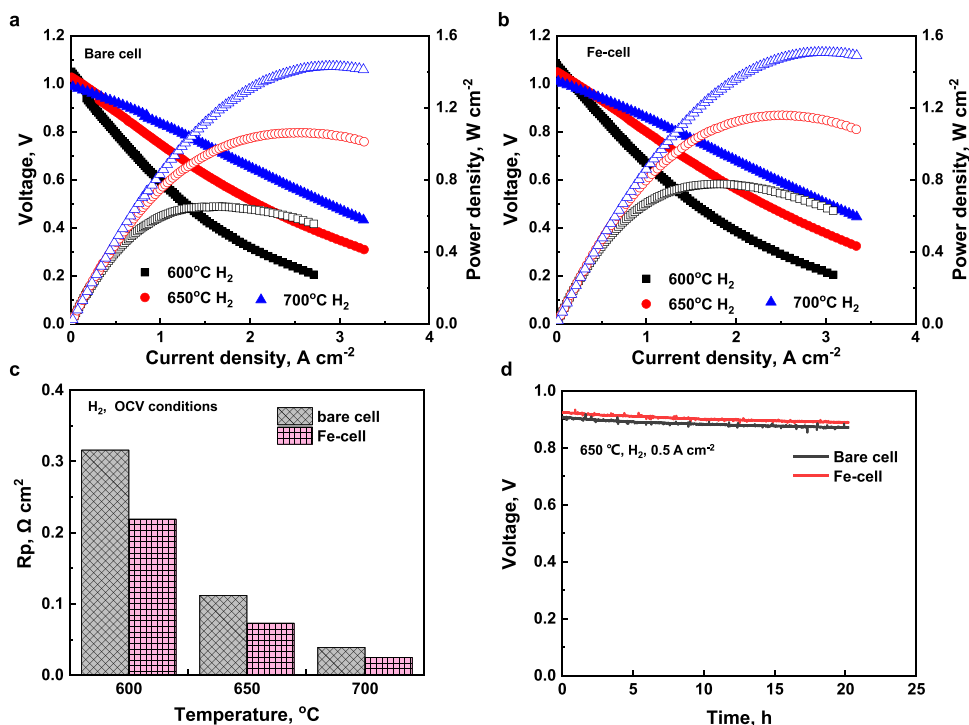


Fig. 3. Electrochemical performances of the tubular cells in pure hydrogen: typical I-V-P curves of (a) the bare cell and (b) the Fe-cell; (c) comparison of polarization resistances of the bare cell and the Fe-cell under OCV conditions; (d) a short term stability tests of 20 h for the bare cell and the Fe-cell at 650 °C under a current density of 0.5 A cm^{-2} .

Fig. 2d. According to the literature, the catalytic decomposition of ammonia over iron can be regarded as two parallel reactions: ammonia catalytic decomposition and nitridation of iron [34]. Phase diagram of a Fe-N system [35] hints that in the cell operation condition (600 ~ 700 °C) ϵ -Fe₂N could be the main form of iron nitrides. The formation of ϵ -Fe₂N was verified by characterizing the XRD patterns of the Fe-cell anodes after the electrochemical testing in ammonia, as shown in Fig. S1a, confirming the reaction between iron and ammonia. Meanwhile, the XRD patterns of the bare cell anodes after electrochemical testing in hydrogen and ammonia were also compared in Fig. S1b. However, these two patterns delivered no obvious differences, implying that nickel nitride was not detected.

3.2. Electrochemical performances of the tubular cells

Single-cell tests fueled by pure hydrogen were conducted on tubular cells without and with the Fe layer, denoted as bare cell and Fe-cell. The related electrochemical performances of the bare cell and the Fe-cell were presented in Fig. 3. Peak power densities (PPDs) of 0.650, 1.060, and 1.429 W cm⁻² were achieved from the bare cell measured at 600, 650, and 700 °C, respectively (Fig. 3a). These were very outstanding performances compared to other proton-conducting tubular SOFCs [36–41] (see Table 1). In the case of the Fe-cell, slightly increased PPDs of 0.776, 1.157, and 1.507 W cm⁻² were found at 600, 650, and 700 °C, respectively (Fig. 3b). Since all conditions were kept the same for the bare cell and the Fe-cell, the performance enhancement can be attributed to the addition of the iron layer. To further compare the electrochemical performances, electrochemical impedance spectra (EIS) of the two tubular cells were investigated under OCV conditions at various temperatures (see Fig. S2). The polarization resistance (R_p) of the two cells can be roughly determined from EIS results, and the values were compared and presented in Fig. 3c. The Fe-cell showed small polarization resistances of 0.219, 0.073, and 0.025 Ω cm² at the temperature of 600, 650, and 700 °C, respectively, which were generally 35% smaller than the polarization resistances of the bare cell at various temperatures. Further electrochemical testings on the Fe-cells and the bare cells verified that the smaller polarization resistances in the Fe-cells were repeatable (Fig. S3). The analysis of frequency behavior suggests that anode reaction activity may be enhanced in the Fe-cells. In conclusion, the enhanced power densities of the Fe-cell can be attributed to the much smaller polarization resistances. In addition to power output, cell durability is also of great significance for SOFCs. The Fe-cell and the bare cell presented very similar stability behaviors in the durability testing when the cell was fueled by hydrogen under a constant current density of 0.5 A cm⁻² at 650 °C. The Fe-cell delivered a slightly higher voltage during the testing period (see Fig. 3d), which further confirms that the catalytic iron layer has little negative impact on the electrochemical performances of our tubular cells when fueled by pure hydrogen.

Electrochemical performances of both tubular cells in ammonia were

characterized after the cells were tested in hydrogen and the results were presented in Fig. 4. When the fuel was switched from pure hydrogen to pure ammonia, there was a sudden drop in open-circuit voltage (OCV). It took a few minutes for the OCV values to recover, although the final values in ammonia were unable to return to the original values in hydrogen. Severe declines of OCV were found in the bare cell when fuel gas was switched from hydrogen to ammonia, more so at lower temperatures (dropped from 0.988 V to 0.947 V at 700 °C, from 1.028 V to 0.948 V at 650 °C, from 1.051 V to 0.918 V at 600 °C). The severe changes of OCV might be related to the insufficient ammonia decomposition catalytic activity of the bare cell. It was confirmed by the ammonia conversion rates during cell testing, as shown in Fig. S4. The ammonia conversion rates in the bare cell were only 61% and 76% at 600 and 650 °C. As a result, insufficient hydrogen was produced at low temperatures, causing difficulty in maintaining high OCV values. Since ammonia decomposition is an endothermic reaction, the bare cell delivered a relatively high ammonia conversion rate at 700 °C (91.5%), coinciding with the smaller decline of OCV at 700 °C. Even though the Fe-cell also underwent drops of OCV when fuel gas was switched to pure ammonia, the changes were less severe (dropped from 1.01 V to 0.99 V at 700 °C, from 1.05 V to 1.011 V at 650 °C, from 1.077 V to 1.011 V at 600 °C). It can be attributed to the much higher ammonia conversion rates in the Fe-cell (Fig. S4), indicating that the iron layer in the Fe-cell indeed improved the catalytic activity of cells toward NH₃ decomposition.

Performance of the bare cell decreased significantly in ammonia, only delivering PPDs of 0.186, 0.506, and 0.994 W cm⁻² at 600, 650, and 700 °C respectively (Fig. 4a). The decreased performance can be partly attributed to the diluted effect of nitrogen. Similarly, such performance decrease was also observed in the Fe-cells in ammonia, as shown by the lower power outputs and larger resistances (Fig. 4b and c). Still, the power outputs in ammonia were higher than those of the bare cells, achieving PPDs of 0.327, 0.685, and 1.078 W cm⁻² at 600, 650, and 700 °C respectively. Notably, the performance enhancement of the Fe-cell over the bare cell was more pronounced at lower temperatures: the PPDs of the Fe-cell in ammonia were 75.8%, 35.4%, and 8.5% higher than those of the bare cell at the temperatures of 600, 650, and 700 °C respectively. The same tendency can be found in the OCV differences of the two cells in ammonia (the Fe-cell versus the bare cell: 1.011 V versus 0.918 V at 600 °C, 1.011 V versus 0.948 V at 650 °C, and 0.99 V versus 0.947 V at 700 °C). It can be concluded that when the tubular cells operated in ammonia, the catalytic iron layer played a more vital role in enhancing the performances at lower temperatures, as the endothermic ammonia decomposition reaction was more sensitive to the catalyst at lower temperatures. Listed in Table 1 is the PPDs comparison of PCFCs when fueled by ammonia in recent studies [42–44], indicating that performances of our Fe-cell were very competitive.

Shown in Fig. 4d are the short-term stability tests of the bare cell and the Fe-cell under a constant current density of 0.5 A cm⁻² at 650 °C when

Table 1

Electrochemical performances of some PCFCs fueled by hydrogen or ammonia in the literatures. (LSCF: La_{0.6}Sr_{0.4}Co_{0.2}Fe_{0.8}O_{3-δ}, SDC: Sm_{0.2}Ce_{0.8}O_{2-δ}, BZCY: BaZr_{0.1}Ce_{0.7}Y_{0.2}O_{3-δ}, BZY: BaZr_{0.8}Y_{0.2}O_{3-δ}, PBC: PrBaCo₂O_{5+δ}, BZCYYbPd: Ba(Zr_{0.1}Ce_{0.7}Y_{0.1}Yb_{0.1})_{0.95}Pd_{0.05}O_{3-δ}, BCFZY: BaCo_{0.4}Fe_{0.4}Zr_{0.1}Y_{0.1}O_{3-δ}, BCY: BaCe_{0.8}Y_{0.2}O_{3-δ}, BSFC: Ba_{0.5}Sr_{0.5}Co_{0.8}Fe_{0.2}O_{3-δ}).

Structure	Electrolyte	Thickness (μm)	Cathode	Temperature (°C)	PPD (mW cm ⁻²)	Ref
Tubular	BZCYYb	12	LSCF-SDC	700	976 (H ₂)	[36]
Tubular	BZCYYb	12	LSCF-BZCYYb	700	810 (H ₂)	[37]
Tubular	BZCY	10	LSCF-BZCY	700	500 (H ₂)	[38]
Tubular	BZCYYb	8	PBSCF	700	1507 (H₂)	This work
Tubular	BZY	20	PBC-BZY	650	327 (H ₂)	[39]
Tubular	BZCYYb	20	LSCF-BZCYYb	650	450 (H ₂)	[40]
Tubular	BZCYYb	12	LSCF	650	721 (H ₂)	[41]
Tubular	BZCYYb	8	PBSCF	650	1157 (H₂)	This work
Planar	BZCYYbPd	17	BCFZY	650	724 (NH ₃)	[42]
Planar	BCY	50	BSCF	650	190 (NH ₃)	[43]
Planar	BZCY	35	BSCF	650	275 (NH ₃)	[44]
Tubular	BZCYYb	8	PBSCF	650,700	685 (NH₃)1078 (NH₃)	This work

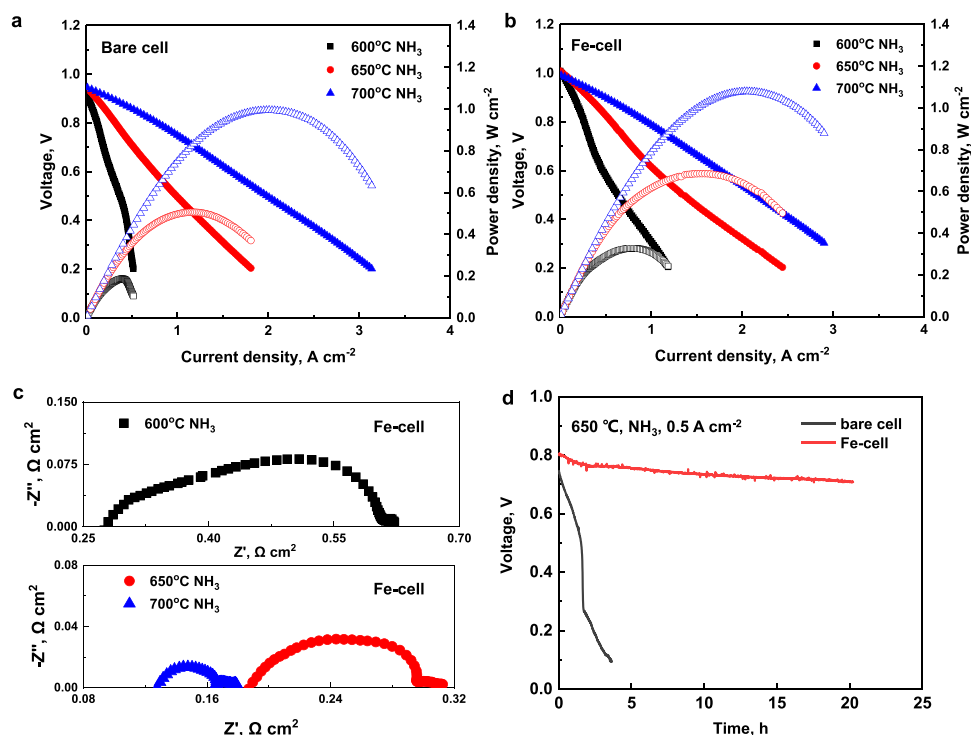


Fig. 4. Electrochemical performances of the tubular cells in pure ammonia: typical I-V-P curves of (a) the bare cell and (b) the Fe-cell; (c) electrochemical impedance spectra of the Fe-cell under OCV conditions; (d) short-term stability tests of the bare cell and the Fe-cell at 650 °C under a constant current density of 0.5 A cm⁻².

fueled by ammonia. A sharp degradation occurred to the bare cell as the voltage dropped from 0.749 V to 0.096 V within only 4 h. The degradation was found to be largely attributed to the increase in ohmic resistance (Fig. S5), which is mainly attributed to the degradation of anode caused by ammonia. The damage of ammonia on the cell can also be observed from the anode microstructure, as shown in Fig. S6. Anode microstructures of the bare cells and the Fe-cell, especially the morphologies of nickel surfaces, were compared after electrochemical testing. Fig. S6a presented the anode microstructure of the bare cell after 20 h testing in hydrogen and the nickel particles were further examined in Fig. S6b, where an ordinary morphology of nickel surface was observed. However, severe morphology changes occurred to the nickel surface after only 4 h operation in ammonia. As shown in Fig. S6c and d, lots of nano-sized pores were found on the nickel surface, which may be related to the interaction between ammonia and nickel particles. Nitridation of nickel particles happened in an ammonia atmosphere. Meanwhile, nickel nitrides can be easily decomposed due to their low stability in a reducing atmosphere or at high temperatures (over 400 °C) [45]. In other words, nickel nitrides existed as a transient state and there was a repeat of nitride formation and decomposition, which might explain the inability to detect nickel nitride in the bare cell after electrochemical testing in ammonia in Fig. S1. The continuous transition inevitably caused structural changes to the nickel particles and nano-sized pores were thereby formed on the surface.

On the other hand, the Fe-cell presented a very different stability behavior in ammonia. Although a rapid degradation was also found in the initial stage of testing, the Fe-cell maintained a relatively stable operation for almost 20 h, indicating that the catalytic iron layer significantly increased the stability of our tubular cells during the operation in ammonia fuel. The benefits of the iron layer were also demonstrated by the morphology of the nickel surface in Fig. S6e and f. The microstructure was very similar to the cell tested in hydrogen and almost no nano-sized pores were formed on the nickel surface. It demonstrates that the anode of the Fe-cell is well protected by the catalytic layer and therefore ammonia had little impact on the morphology of nickel.

3.3. DFT studies of the Fe-cell durability in ammonia

Based on the experimental findings, we assumed that the effect of the iron layer can be schematically demonstrated in Fig. S7. Briefly, in the bare cell, ammonia is directly fed to the Ni-BZCYb anode, followed by the catalytic decomposition to hydrogen over active nickel surfaces. As aforementioned, transient nickel nitrides would be formed and decomposed repeatedly via surface and bulk reactions, resulting in a dramatic morphology change (Fig. S6d). These phenomena are difficult to observe using *ex-situ* characterization approaches. Thus, we investigated its electronic properties using DFT calculations. We assumed that the severe microstructural change of the bare cell after exposure to ammonia fuel is irreversible, suggesting that the surface nitridation ($x\text{Ni} + \text{NH}_3 \leftrightarrow \text{Ni}_x\text{N} + 3/2 \text{H}_2$ and $\text{Ni}_x\text{N} \leftrightarrow x\text{Ni} + 1/2 \text{N}_2$) becomes a bulk reaction (which is confirmed by the operation of the bare cells in ammonia for a different period, as shown in Fig. S8). Then, it could cause a detrimental impact on the anode structure and the degradation of cell performances. It was reported that its continuous volumetric changes of nickel particles [20] cause severe cracks. We approximated the volumetric changes using DFT calculations as described below. The catalytic iron layer of the Fe-cell may also experience a similar nitridation for the formation of Fe_xN ($x\text{Fe} + \text{NH}_3 \rightarrow \text{Fe}_x\text{N} + 3/2 \text{H}_2$). In this configuration, we assume that the ammonia decomposition reaction mainly takes place on the additional iron layer. A small amount of NH_3 would reach the interfacial areas between the iron layer and Ni-BZCYb anode (defined as FeNi region) due to the porous microstructure (Fig. 2c) along with hydrogen molecules decomposed from ammonia ($\text{NH}_3 \rightarrow 1/2 \text{N}_2 + 3/2 \text{H}_2$). Based on this observation, as summarized in Fig. 5, to theoretically elucidate the augmented stability of the Fe-cell compared to the bare cell by minimizing the direct interaction between nickel anodes and ammonia fuel, first-principles-based thermodynamic calculations were performed below. It supports the iron layer effectively limits the formation of nickel nitrides, improving the cell stability. As shown in Figs. 5 and S9, three surface models of Ni(111), FeNi(111), and Fe(110) were constructed to examine the adsorption characteristics of atomic nitrogen because it can be accurately applied as a descriptor for the rational design of catalytic

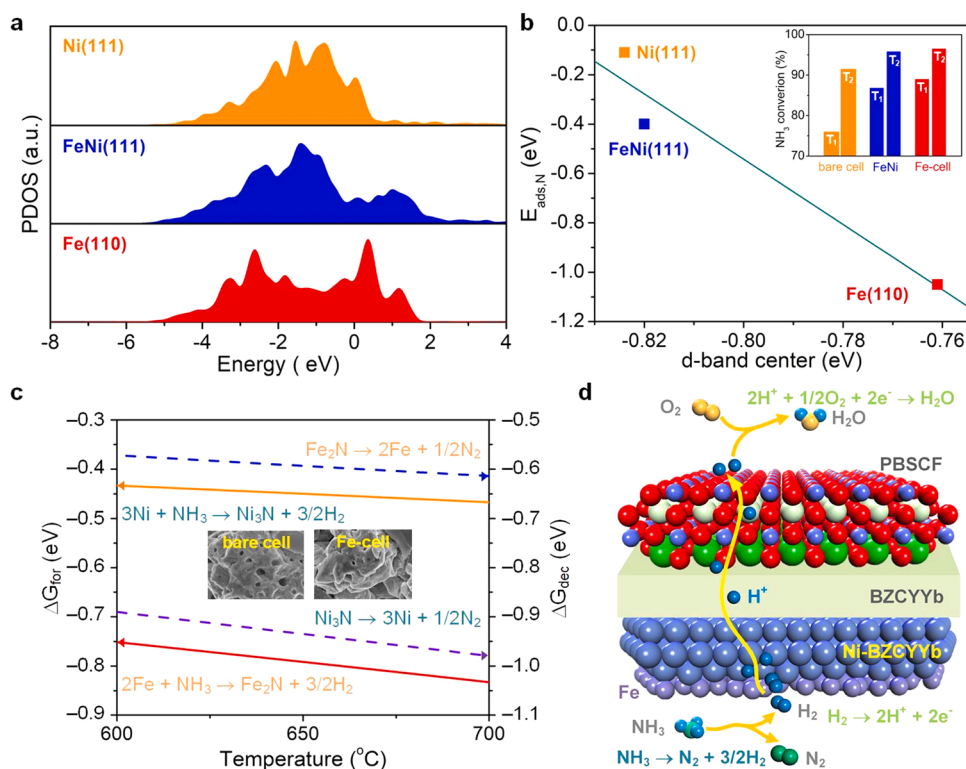


Fig. 5. (a) Projected density of states (PDOSs) of the d-orbitals of Ni(111), FeNi(111), and Fe(110). The Fermi energy level (E_F) is set to zero. (b) Adsorption energy of atomic nitrogen on Ni(111), FeNi(111), and Fe(110) against their d-band center. The inset of the figure is the experimental NH₃ conversion (%) for the bare cell, FeNi, and Fe-cell measured at 650 °C (T_1) and 700 °C (T_2). (c) Gibbs free energy changes of the formation (ΔG_{for} (eV)) and decomposition (ΔG_{dec} (eV)) of Ni₃N and Fe₂N from 600 °C to 700 °C. The SEM images are for the bare cell and the Fe-cell after NH₃-fueled experiments. (d) A schematic illustration of an ammonia-fueled PCFC using the iron layer.

materials for ammonia decomposition [46,47]. Briefly, based on DFT calculations, the initial adsorption of NH₃ through nitrogen to a catalytic surface and the reaction barrier height for desorption of a nitrogen molecule (*i.e.*, association reaction of nitrogen species for producing gas-phase nitrogen) are strongly dependent on an amount of nickel and iron loadings. The more iron atoms on catalyst surfaces exhibit stronger adsorption of ammonia and the higher desorption barrier of nitrogen. Our detailed measurements of NH₃ conversion on the three different anode materials in Fig. S4 clarify that the Fe-cell exhibits the best activity towards NH₃ decomposition, while the FeNi alloy's conversion is close to that of the Fe-cell at 700 °C. This may denote the significance of initial NH₃'s adsorption energy and desorption barrier heights of nitrogen molecules. Fig. 5a displays the calculated projected density of states (PDOSs) of the d-orbitals of three bare surfaces of Ni(111), FeNi(111), and Fe(110). We assume that FeNi(111) could be considered as interfacial moieties between Ni and Fe or the Ni-BZCYYb anode and the iron layer (Fig. 2c). We compared the adsorption energy of atomic nitrogen as a descriptor for understanding the efficient NH₃ decomposition and desorption of nitrogen products. Summarized in Fig. 5b is an excellent linear relationship of d-band centers and adsorption energies of atomic nitrogen and the experimental NH₃ conversion in our experimental temperature range. It indicates that the iron layer catalytically improves the NH₃ decomposition reaction. As Fe also has a good catalytic activity to hydrogen dissociation [48], we experimentally compared the NH₃ conversion by mixing nickel and iron oxides, followed by reduction (Figs. S3 and 5b). It indirectly explains that the interfacial FeNi regions are effectively utilized for the decomposition of ammonia passing through the porous iron layer and hydrogen dissociation ($\text{H}_2 \rightarrow 2\text{H}$). Since these reactions take place on the catalyst surfaces, we further investigated bulk nitride formation. Due to the unavailability of accurate thermodynamic properties of nitrides of nickel and iron, we carried out first-principles based Gibbs free energy calculations under the experimental temperature range of 600 °C and 700 °C (Fig. 5c) by assuming representative nickel and iron nitrides are Ni₃N and Fe₂N, respectively [35,49]. Gibbs energy changes denote that Fe₂N can be more easily formed than Ni₃N via nitridation, while the

decomposition of Ni₃N occurs more spontaneously than Fe₂N in reduction conditions ($\text{Ni}_3\text{N} + 3/2\text{H}_2 \rightarrow 3\text{Ni} + \text{NH}_3$) and via the thermal decomposition reaction ($\text{Ni}_3\text{N} \rightarrow 3\text{Ni} + 1/2\text{N}_2$). As mentioned above, we observed Fe₂N only after carrying out NH₃-fueled experiments (Fig. S1). Therefore, as compared in Figs. 5c and S6, one could conclude that the spontaneous reversible reactions of nickel versus nickel nitrides can cause irreversible alteration of microstructures of anode materials owing to the volume change of the unit cells of nickel and nickel nitrides (*i.e.*, 21.8% of Ni versus Ni₃N) (Table S1). In summary, the iron layer effectively minimizes the direct interaction of ammonia and nickel anodes, inhibiting nitride formation and resulting in outstanding stability. Furthermore, the synergistic contribution for hydrogen dissociation on Ni, FeNi interfaces, and Fe improves the overall performance compared to the bare cell. Its schematic illustration of the overall NH₃-fueled PCFC is displayed in Fig. 5d.

4. Conclusion

Tubular PCFCs based on the Ni-BZCYYb anode support have been successfully fabricated by adding an internal layer of iron to its inner side. The electrochemical performances of the tubular cells with and without the iron layer (denoted as Fe-cell and bare cell, respectively) have been compared to evaluate the effect of iron. When fueled by pure hydrogen, high PPDs of 0.776, 1.157, and 1.507 W cm⁻² were achieved by the Fe-cell at the temperatures of 600, 650, and 700 °C, respectively, which were slightly higher than the PPDs of the bare cell. Long-term tests of both cells under a constant current density of 0.5 A cm⁻² at 650 °C demonstrated that the Fe-cell and the bare cell showed a similar stability behavior in hydrogen. When fuel gas was switched to pure ammonia, PPDs of the Fe-cell were 0.327, 0.685, and 1.078 W cm⁻² at the temperatures of 600, 650, and 700 °C, respectively. Compared to the bare cell, the Fe-cell delivered much higher power outputs, especially at lower temperatures. In particular, the stability of the cell on ammonia was greatly enhanced by the catalytic iron layer, while a sharp degradation occurred to the bare cell within only a few hours during long-term testing. The outstanding enhancement of the stability is

attributed to the increased catalytic ammonia decomposition activity and the protective effect of the iron layer.

CRediT authorship contribution statement

Yuxin Pan: Investigation, Data curation, Visualization, Writing – original draft. **Hua Zhang:** Investigation. **Kang Xu:** Investigation. **Yucun Zhou:** Writing – review & editing. **Bote Zhao:** Writing – review & editing. **Wei Yuan:** Writing – review & editing. **Kotaro Sasaki:** Writing – review & editing. **YongMan Choi:** Software, Resources, Writing – review & editing. **Yu Chen:** Conceptualization, Writing – review & editing, Project administration, Funding acquisition. **Meilin Liu:** Writing – review & editing.

Declaration of Competing Interest

The authors declare that they have no known competing financial interests or personal relationships that could have appeared to influence the work reported in this paper.

Acknowledgments

This work was supported by the National Natural Science Foundation of China (22005105, 22179039), the Pearl River Talent Recruitment Program (2019QN01C693, and 2021ZT09L392), and the Natural Science Foundation of Guangdong Province (2021A1515010395). Computational studies were supported by the Ministry of Science and Technology of Taiwan (MOST Grant No. 110–2221-E-A49–017-MY3), the National Center for High-performance Computing (NCHC), and the Higher Education Sprout Project of the National Yang Ming Chiao Tung University and Ministry of Education (MOE), Taiwan. DFT calculations were performed using the resources of the Center for Functional Nanomaterials, which is a U.S. DOE Office of Science Facility, at Brookhaven National Laboratory under Contract No. DE-SC0012704, Taiwan.

Appendix A. Supporting information

Supplementary data associated with this article can be found in the online version at [doi:10.1016/j.apcatb.2022.121071](https://doi.org/10.1016/j.apcatb.2022.121071).

References

- [1] E.P. Murray, T. Tsai, S.A. Barnett, A direct-methane fuel cell with a ceria-based anode, *Nature* 400 (1999) 649–651.
- [2] Z. Shao, S.M. Haile, A high-performance cathode for the next generation of solid-oxide fuel cells, *Nature* 431 (2004) 170–173.
- [3] Y. Zhang, B. Chen, D. Guan, M. Xu, R. Ran, M. Ni, W. Zhou, R. O'Hayre, Z. Shao, Thermal-expansion offset for high-performance fuel cell cathodes, *Nature* 591 (2021) 246–251.
- [4] Y. Chen, Y. Chen, D. Ding, Y. Ding, Y. Choi, L. Zhang, S. Yoo, D. Chen, B. deGlee, H. Xu, Q. Lu, B. Zhao, G. Vardar, J. Wang, H. Bluhm, E.J. Crumlin, C. Yang, J. Liu, B. Yildiz, M. Liu, A robust and active hybrid catalyst for facile oxygen reduction in solid oxide fuel cells, *Energy Environ. Sci.* 10 (2017) 964–971.
- [5] C. Duan, R.J. Kee, H. Zhu, C. Karakaya, Y. Chen, S. Ricote, A. Jarry, E.J. Crumlin, D. Hook, R. Braun, N.P. Sullivan, R. O'Hayre, Highly durable, coking and sulfur tolerant, fuel-flexible protonic ceramic fuel cells, *Nature* 557 (2018) 217–222.
- [6] S. Sengodan, S. Choi, A. Jun, T.H. Shin, Y.-W. Ju, H.Y. Jeong, J. Shin, J.T.S. Irvine, G. Kim, Layered oxygen-deficient double perovskite as an efficient and stable anode for direct hydrocarbon solid oxide fuel cells, *Nat. Mater.* 14 (2015) 205–209.
- [7] Y. Chen, B. deGlee, Y. Tang, Z. Wang, B. Zhao, Y. Wei, L. Zhang, S. Yoo, K. Pei, J. H. Kim, Y. Ding, P. Hu, F.F. Tao, M. Liu, A robust fuel cell operated on nearly dry methane at 500 °C enabled by synergistic thermal catalysis and electrocatalysis, *Nat. Energy* 3 (2018) 1042–1050.
- [8] Y. Chen, Y. Choi, S. Yoo, Y. Ding, R. Yan, K. Pei, C. Qu, L. Zhang, I. Chang, B. Zhao, Y. Zhang, H. Chen, Y. Chen, C. Yang, B. deGlee, R. Murphy, J. Liu, M. Liu, A highly efficient multi-phase catalyst dramatically enhances the rate of oxygen reduction, *Joule* 2 (2018) 938–949.
- [9] A.M. Abdalla, S. Hossain, O.B. Nisfindy, A.T. Azad, M. Dawood, A.K. Azad, Hydrogen production, storage, transportation and key challenges with applications: a review, *Energy Convers. Manag.* 165 (2018) 602–627.
- [10] G. Pettipas, Simulation of boil-off losses during transfer at a LH₂ based hydrogen refueling station, *Int. J. Hydrog. Energy* 43 (2018) 21451–21463.
- [11] A. Wojcik, H. Middleton, I. Damopoulos, J.V. Herle, Ammonia as a fuel in solid oxide fuel cells, *J. Power Sources* 118 (2003) 342–348.
- [12] J. Yang, T. Akagi, T. Okanishi, H. Muroyama, T. Matsui, K. Eguchi, Catalytic influence of oxide component in Ni-based cermet anodes for ammonia-fueled solid oxide fuel cells, *Fuel Cells* 15 (2015) 390–397.
- [13] A. Klerke, C.H. Christensen, J.K. Nørskov, T. Vegge, Ammonia for hydrogen storage: challenges and opportunities, *J. Mater. Chem.* 18 (2008) 2304–2310.
- [14] A. Valera-Medina, H. Xiao, M. Owen-Jones, W.I.F. David, P.J. Bowen, Ammonia for power, *Prog. Energy Combust. Sci.* 69 (2018) 63–102.
- [15] K. Xie, Q. Ma, B. Lin, Y. Jiang, J. Gao, X. Liu, G. Meng, An ammonia fuelled SOFC with a BaCe_{0.9}Nd_{0.1}O_{3-δ} thin electrolyte prepared with a suspension spray, *J. Power Sources* 170 (2007) 38–41.
- [16] Y. Aoki, T. Yamaguchi, S. Kobayashi, D. Kowalski, C. Zhu, H. Habazaki, High-efficiency direct ammonia fuel cells based on BaZr_{0.1}Ce_{0.7}Y_{0.2}O_{3-δ}/Pd oxide-metal junctions, *Global Chall.* 2 (2018) 1700088.
- [17] J. Yang, A.F.S. Molouk, T. Okanishi, H. Muroyama, T. Matsui, K. Eguchi, Electrochemical and catalytic properties of Ni/BaCe_{0.75}Y_{0.25}O_{3-δ} anode for direct ammonia-fueled solid oxide fuel cells, *ACS Appl. Mater. Interfaces* 7 (2015) 7406–7412.
- [18] M. Ni, D.Y.C. Leung, M.K.H. Leung, Thermodynamic analysis of ammonia fed solid oxide fuel cells: comparison between proton-conducting electrolyte and oxygen ion-conducting electrolyte, *J. Power Sources* 183 (2008) 682–686.
- [19] Z. Wan, Y. Tao, J. Shao, Y. Zhang, H. You, Ammonia as an effective hydrogen carrier and a clean fuel for solid oxide fuel cells, *Energy Convers. Manag.* 228 (2021), 113729.
- [20] J. Yang, A.F.S. Molouk, T. Okanishi, H. Muroyama, T. Matsui, K. Eguchi, A stability study of Ni/Yttria-stabilized zirconia anode for direct ammonia solid oxide fuel cells, *ACS Appl. Mater. Interfaces* 7 (2015) 28701–28707.
- [21] W. Wang, C. Su, Y. Wu, R. Ran, Z. Shao, Progress in solid oxide fuel cells with nickel-based anodes operating on methane and related fuels, *Chem. Rev.* 113 (2013) 8104–8151.
- [22] T. Suzuki, T. Yamaguchi, K. Hamamoto, Y. Fujishiro, M. Awano, N. Sammes, A functional layer for direct use of hydrocarbon fuel in low temperature solid-oxide fuel cells, *Energy Environ. Sci.* 4 (2011) 940–943.
- [23] K. Kendall, Progress in microtubular solid oxide fuel cells, *Int. J. Appl. Ceram. Technol.* 7 (2010) 1–9.
- [24] N.M. Sammes, Y. Du, Fabrication and characterization of tubular solid oxide fuel cells, *Int. J. Appl. Ceram. Technol.* 4 (2007) 89–102.
- [25] L. Yang, S. Wang, K. Blinn, M. Liu, Z. Liu, Z. Cheng, M. Liu, Enhanced sulfur and coking tolerance of a mixed ion conductor for SOFCs: BaZr_{0.1}Ce_{0.7}Y_{0.2-*x*}Yb_{*x*}O_{3-δ}, *Science* 326 (2009) 126.
- [26] G. Kresse, J. Hafner, Ab initio molecular dynamics for liquid metals, *Phys. Rev. B* 47 (1993) 558–561.
- [27] G. Kresse, J. Furthmüller, Efficient iterative schemes for ab initio total-energy calculations using a plane-wave basis set, *Phys. Rev. B* 54 (1996) 11169–11186.
- [28] J.P. Perdew, K. Burke, M. Ernzerhof, Generalized gradient approximation made simple, *Phys. Rev. Lett.* 77 (1996) 3865–3868.
- [29] P.E. Blöchl, Projector augmented-wave method, *Phys. Rev. B* 50 (1994) 17953–17979.
- [30] H.J. Monkhorst, J.D. Pack, Special points for brillouin-zone integrations, *Phys. Rev. B* 13 (1976) 5188–5192.
- [31] A. Nilsson, L.G.M. Pettersson, B. Hammer, T. Bligaard, C.H. Christensen, J. K. Nørskov, The electronic structure effect in heterogeneous catalysis, *Catal. Lett.* 100 (2005) 111–114.
- [32] B. Delley, An all-electron numerical method for solving the local density functional for polyatomic molecules, *J. Chem. Phys.* 92 (1990) 508–517.
- [33] H. Strathmann, K. Kock, The formation mechanism of phase inversion membranes, *Desalination* 21 (1977) 241–255.
- [34] W. Arabczyk, R. Pelka, Studies of the kinetics of two parallel reactions: ammonia decomposition and nitriding of iron catalyst, *J. Phys. Chem. A* 113 (2) (2009) 411–416.
- [35] B.J. Kooi, M.A.J. Somers, E.J. Mittemeijer, An evaluation of the Fe-N phase diagram considering long-range order of N atoms in γ-Fe₄N_{1-*x*} and ε-Fe₂N_{1-*z*}, *Metall. Mater. Trans. A* 27 (1996) 1063–1071.
- [36] C. Chen, Y. Dong, L. Li, Z. Wang, M. Liu, B.H. Rainwater, Y. Bai, Electrochemical properties of micro-tubular intermediate temperature solid oxide fuel cell with novel asymmetric structure based on BaZr_{0.1}Ce_{0.7}Y_{0.1}Yb_{0.1}O_{3-δ} proton conducting electrolyte, *Int. J. Hydrog. Energy* 44 (2019) 16887–16897.
- [37] C. Chen, M. Liu, Y. Bai, L. Yang, E. Xie, M. Liu, Anode-supported tubular SOFCs based on BaZr_{0.1}Ce_{0.7}Y_{0.1}Yb_{0.1}O_{3-δ} electrolyte fabricated by dip coating, *Electrochem. Commun.* 13 (2011) 615–618.
- [38] S.H. Min, R.-H. Song, J.G. Lee, M.-G. Park, K.H. Ryu, Y.-K. Jeon, Y.-G. Shul, Fabrication of anode-supported tubular Ba(Zr_{0.1}Ce_{0.7}Y_{0.2})O_{3-δ} cell for intermediate temperature solid oxide fuel cells, *Ceram. Int.* 40 (2014) 1513–1518.
- [39] L. Bi, E.H. Da'as, S.P. Shafi, Proton-conducting solid oxide fuel cell (SOFC) with Y-doped BaZrO₃ electrolyte, *Electrochem. Commun.* 80 (2017) 20–23.
- [40] C. Ren, S. Wang, T. Liu, Y. Lin, F. Chen, Fabrication of micro-tubular solid oxide fuel cells using sulfur-free polymer binder via a phase inversion method, *J. Power Sources* 290 (2015) 1–7.
- [41] Y. Dong, C. Chen, M. Liu, B.H. Rainwater, Y. Bai, Enhancement of electrochemical properties, impedance and resistances of micro-tubular IT-SOFCs with novel asymmetric structure based on BaZr_{0.1}Ce_{0.7}Y_{0.1}Yb_{0.1}O_{3-δ} proton conducting electrolyte, *Fuel Cells* 20 (2020) 70–79.
- [42] F. He, Q. Gao, Z. Liu, M. Yang, R. Ran, G. Yang, W. Wang, W. Zhou, Z. Shao, A. New, A new Pd doped proton conducting perovskite oxide with multiple

- functionalities for efficient and stable power generation from ammonia at reduced temperatures, *Adv. Energy Mater.* 11 (2021) 2003916.
- [43] Y. Yoo, M. Tuck, N. Lim, A. McFarlan, N. Maffei, Fabrication of anode supported direct ammonia solid oxide fuel cells based on proton conducting Y-doped BaCeO₃ electrolyte, *ECS Trans.* 7 (2019) 2305–2312.
- [44] Y. Lin, R. Ran, Y. Guo, W. Zhou, R. Cai, J. Wang, Z. Shao, Proton-conducting fuel cells operating on hydrogen, ammonia and hydrazine at intermediate temperatures, *Int. J. Hydrog. Energy* 35 (2010) 2637–2642.
- [45] A. Baiker, M. Maciejewski, Formation and thermal stability of copper and nickel nitrides, *J. Chem. Soc. Faraday Trans. 1: Phys. Chem. Condens. Ph.* 80 (1984) 2331–2341.
- [46] X. Duan, G. Qian, C. Fan, Y. Zhu, X. Zhou, D. Chen, W. Yuan, First-principles calculations of ammonia decomposition on Ni(110) surface, *Surf. Sci.* 606 (2012) 549–553.
- [47] X. Duan, J. Ji, G. Qian, C. Fan, Y. Zhu, X. Zhou, D. Chen, W. Yuan, Ammonia decomposition on Fe(110), Co(111) and Ni(111) surfaces: a density functional theory study, *J. Mol. Catal. A-Chem.* 357 (2012) 81–86.
- [48] Z. Cheng, J.-H. Wang, Y. Choi, L. Yang, M.C. Lin, M. Liu, From Ni-YSZ to sulfur-tolerant anode materials for SOFCs: electrochemical behavior, in situ characterization, modeling, and future perspectives, *Energy Environ. Sci.* 4 (2011) 4380–4409.
- [49] A. Fernández Guillermet, K. Frisk, Thermodynamic properties of Ni nitrides and phase stability in the Ni-N system, *Int. J. Thermophys.* 12 (1991) 417–431.